



# Enhanced photocatalytic mechanism of $\text{Ag}_3\text{PO}_4$ nano-sheets using $\text{MS}_2$ ( $\text{M} = \text{Mo, W}$ )/rGO hybrids as co-catalysts for 4-nitrophenol degradation in water



Weiping Zhang<sup>a</sup>, Guiying Li<sup>a</sup>, Wanjun Wang<sup>a</sup>, Yixin Qin<sup>a</sup>, Taicheng An<sup>a,\*</sup>, Xinyan Xiao<sup>b,\*</sup>, Wonyong Choi<sup>a,c</sup>

<sup>a</sup> *Guangzhou Key Laboratory of Environmental Catalysis and Pollution Control, Institute of Environmental Health and Pollution Control, School of Environmental Science and Engineering, Guangdong University of Technology, Guangzhou, 510006, China*

<sup>b</sup> *School of Chemistry and Chemical Engineering, South China University of Technology, Guangzhou 510640, China*

<sup>c</sup> *Division of Environmental Science and Engineering, Pohang University of Science and Technology (POSTECH), Pohang 37673, Republic of Korea*

## ARTICLE INFO

### Keywords:

Photocatalyst  
Silver phosphate  
Reduced graphene oxide  
Transition metal disulfide  
Organic pollutant degradation

## ABSTRACT

A chemically modified  $\text{Ag}_3\text{PO}_4@\text{MS}_2(\text{M} = \text{Mo, W})/\text{rGO}$  composite was firstly synthesized via a liquid-exfoliation solvothermal method. The structure, morphology, optical properties and composition were characterized by X-ray diffraction, FT-IR spectroscopy, scanning electron microscopy, UV-vis diffuse reflectance spectra and X-ray photoelectron spectroscopy, respectively. The characterization results indicated that compact structure could be obtained by using this typical method due to in-situ chemical modification, which could also control the sizes of  $\text{Ag}_3\text{PO}_4$  nano-sheets by adding  $\text{MS}_2/\text{rGO}$  hybrids. More importantly, the resultant  $\text{Ag}_3\text{PO}_4@\text{MS}_2/\text{rGO}$  composite exhibited higher photocatalytic activity and stability toward the degradation of 4-nitrophenol than pure  $\text{Ag}_3\text{PO}_4$  under sunlight irradiation. The stable structure of  $\text{Ag}_3\text{PO}_4@\text{MS}_2/\text{rGO}$  was closely related with Z-scheme electronic structure and electrical conductivity of  $\text{MS}_2/\text{rGO}$  hybrids, leading to a higher consumption and transfer of photogenerated electrons. However, by controlling the amounts of  $\text{MS}_2/\text{rGO}$  hybrids, more stable but lower photocatalytic activity composites could be obtained. Further analysis found that the holes and  $\cdot\text{O}_2^-$  were the main reactive species involved in the photocatalytic degradation of 4-nitrophenol. In addition, possible photocatalytic degradation pathways of 4-nitrophenol were also proposed based on the identified intermediates. The findings of this work may provide a new method to design efficient composites for photocatalytic degradation of organic pollutants.

## 1. Introduction

The ultimate aims of water or air purification are the mineralization of organic contaminants to harmless liquid or gaseous inorganic small-molecular compounds. At present, photocatalytic oxidation, as a green technique, has been attracted much attention on the environmental application [1–4]. However, many photocatalysts previously reported cannot oxidize those organic pollutants into harmless compounds, instead, even more toxic intermediates produced. Extensive efforts have therefore been devoted to develop photocatalysts with high powerful oxidizability [5,6]. Silver orthophosphate ( $\text{Ag}_3\text{PO}_4$ ), as one of the efficient photocatalysts, has been attracted much attention on the decomposition of organic pollutants under visible-light irradiation due to its excellent photo-oxidative capacity [7,8]. Moreover, due to its higher oxidation potential, organic molecules can be easily decomposed into

$\text{CO}_2$  and  $\text{H}_2\text{O}$  by  $\text{Ag}_3\text{PO}_4$ , which is considered to be a promising visible-light photocatalyst. However,  $\text{Ag}_3\text{PO}_4$  suffers photocorrosion and then decomposes into weakly active silver due to photo-induced electron reduction during the photocatalytic process.

To inhibit this photocorrosion effect, combining  $\text{Ag}_3\text{PO}_4$  with other metals [9,10] or other semiconductors [11–13] to form hybrid materials is an effective way to promote the electron transfer and thus enhance the photocatalytic stability of  $\text{Ag}_3\text{PO}_4$ . Many researches focused on artificial heterogeneous Z-scheme photocatalytic systems due to their advantages over decreasing the recombination of electron/hole pairs as well as the photocorrosion. Yu et al. demonstrated that the photocatalytic mechanism of Z-scheme photocatalytic system (Z-scheme PS) in their previous report [14]. From their viewpoints, the Z-scheme PS consists of PS1, PS2 and electron mediator. During the photocatalytic reaction, the photogenerated electrons from conduction

\* Corresponding authors.

E-mail addresses: [antc99@163.com](mailto:antc99@163.com), [antc99@gdtu.edu.cn](mailto:antc99@gdtu.edu.cn) (T. An), [cexy>xiao@scut.edu.cn](mailto:cexy>xiao@scut.edu.cn) (X. Xiao).

band (CB) of PS1 can directly consume photogenerated holes from the valence band (VB) of PS2 through an electron mediator, resulting in protecting the PS1 from photo-reduction and suppressing the photo-oxidation of PS2. Thus, Z-scheme PS system through coupling  $\text{Ag}_3\text{PO}_4$  with other matched semiconductor will be a great potential technique to resist the photocorrosion. Fan et al. prepared an  $\text{Ag}_3\text{PO}_4/\text{g-C}_3\text{N}_4$  composite photocatalyst using in-situ deposition method and found that the Z-scheme photocatalyst exhibited high efficiency in the photocatalytic reduction of  $\text{CO}_2$  to fuels [15]. Similar results were also obtained by Yang et al. [16]. Pan et al. also reported a hierarchical flower-like  $\text{Ag}_3\text{PO}_4/\text{SnSe}_2$  composite photocatalyst for the enhanced degradation of Rhodamine B, due to a synergistic effect of Z-scheme PS of  $\text{Ag}_3\text{PO}_4/\text{SnSe}_2$  [17].

Recently, the transition metal sulfides (TMS), such as  $\text{MoS}_2$  and  $\text{WS}_2$ , possessing a narrow band-gap and photocatalytic stability, have attracted much attention on the photocatalytic reactions [18,19]. Extensive researches have demonstrated that single- or few-layered  $\text{MoS}_2$  or  $\text{WS}_2$  has much better photocatalytic performance than bulk materials due to quantum confinement effect [20–22]. The matched energy level of TMS with  $\text{Ag}_3\text{PO}_4$  was likely to form Z-Scheme PS, which can effectively inhibit the reduction of  $\text{Ag}_3\text{PO}_4$  and the oxidation of TMS, resulting in higher photostability. Wang et al. found a three-dimensional  $\text{Ag}_3\text{PO}_4/\text{TiO}_2/\text{MoS}_2$  photocatalyst exhibited excellent anti-photocorrosion performance [23], and Fan et al. found that the photocatalytic activity and photostability of  $\text{Ag}_3\text{PO}_4/\text{MoS}_2$  quantum dot/few-layered  $\text{MoS}_2$  nanosheet heterostructures were much superior to pure  $\text{Ag}_3\text{PO}_4$  nanoparticles under visible light irradiation [24]. On account of the poor electrical conductivity of TMS, the electron-transfer of TMS and  $\text{Ag}_3\text{PO}_4$  would be significantly decreased, leading to poor photoactivity and photostability of this kind photocatalysts.

Due to excellent mobility of charge carriers of graphene, a few researches focused on  $\text{Ag}_3\text{PO}_4$ -graphene-based photocatalyst systems, which were constantly used as electron-acceptor in fabrication of  $\text{Ag}_3\text{PO}_4$ -based photocatalyst [25–27]. Reduced graphene oxide (rGO) contains a range of reactive oxygen functional groups, such as epoxide, hydroxyl, carbonyl and carboxyl groups, which can easily couple with semiconductor photocatalysts to form stable heterostructure, resulting in photogenerated electrons transforming from  $\text{Ag}_3\text{PO}_4$  to carbon chains of rGO and then retarding photocorrosion [28].

Thus, in this work, the  $\text{MS}_2$ ( $\text{MoS}_2$  or  $\text{WS}_2$ )/rGO were matched with  $\text{Ag}_3\text{PO}_4$  with providing a co-catalytic effect, to further enhance the photocatalytic activity and photostability of  $\text{Ag}_3\text{PO}_4$ . The synergistic effect of  $\text{MS}_2$  with rGO could effectively enhance the consumption and transfer of photogenerated electrons through Z-scheme electronic structure and the carbon chains of rGO. Firstly, efficient charge separation could be obtained between  $\text{MS}_2$  and  $\text{Ag}_3\text{PO}_4$  due to their matched band-edges; secondly, the holes from the VB of  $\text{MS}_2$  consume the electrons from the CB of  $\text{Ag}_3\text{PO}_4$ , leading to inhibition of the reduction of  $\text{Ag}_3\text{PO}_4$  into Ag. Thirdly, the photogenerated electrons from the CB of  $\text{MS}_2$  would transfer to carbon chains and react with adsorbed  $\text{O}_2$  then into  $\cdot\text{O}_2^-$ , increasing the oxidation species to decompose organic pollutants. This contribution would provide a new strategy to design and synthesize efficient photocatalyst with high photoactivity and photostability for the environmental application. Additionally, the photocatalytic mechanism of 4-nitrophenol was also investigated based on both the identified reactive species (RSs) and intermediates to trace the transformation mechanism as well as the final fate of organic pollutants in water.

## 2. Experimental section

### 2.1. Materials

Tungsten disulfides ( $\text{WS}_2$ , 99%), Hydroquinone (99%) and benzoquinone (%) were purchased from Aladdin Reagent Co. Ltd. (Shanghai, China). Molybdenum dichalcogenides ( $\text{MoS}_2$ , 99%) were from Tianjin

Fuchen Chemical Reagents Factory (Tianjin, China). Ethanol, 4-nitrophenol, silver nitrate ( $\text{AgNO}_3$ , 99.7%) and  $\text{Na}_2\text{HPO}_4 \cdot 12\text{H}_2\text{O}$  were from Sinopharm Chemical Reagent Co. Ltd. (Shanghai, China). Glycerol and graphite powders (99.0%) were from Tianjin Kemiou Chemical Reagent Co. Ltd. (Tianjin, China). 2,4-Dinitrophenol (2,4-DNP) was purchased from Guangzhou Chemical Reagent (Guangzhou, China). All reagents were used as received without any further treatment, and the solutions were freshly prepared with - deionized water.

### 2.2. Synthesis and characterizations of $\text{Ag}_3\text{PO}_4@\text{MS}_2$ ( $\text{M} = \text{Mo, W}$ )/rGO nanocomposites

Graphene oxide was synthesized from graphite via Hummers' method [29], and the rGO was prepared through according to our previous work [30].  $\text{Ag}_3\text{PO}_4@\text{MS}_2$ ( $\text{M} = \text{Mo, W}$ )/rGO composites were synthesized with a two-step solvothermal process. Firstly, the hybrids of  $\text{MS}_2$ /rGO were synthesized by a liquid-exfoliation solvothermal treatment with layered  $\text{MS}_2$  and rGO in water/ethanol solution at 80 °C for 15 h. Subsequently,  $\text{Ag}_3\text{PO}_4@\text{MS}_2$ /rGO nanocomposites were synthesized by an in-situ deposition- solvothermal method of 140 °C for 15 h using  $\text{MS}_2$ /rGO as the co-catalyst, with  $\text{AgNO}_3$  and  $\text{Na}_2\text{HPO}_4 \cdot 12\text{H}_2\text{O}$  as raw materials. The tawny precipitate of  $\text{Ag}_3\text{PO}_4@\text{MS}_2$ /rGO was collected by centrifugation at 5000 rpm for 5 min and then washed repeatedly with water/ethanol solution (volume ratio = 1:1) for several times. The powder samples were finally dried in an oven at 60 °C for 5 h. The  $\text{Ag}_3\text{PO}_4$ - $\text{MS}_2$ -rGO composites with different  $\text{MS}_2$ /rGO contents are denoted as  $\text{AgM1.5rGO2.5}$ ,  $\text{AgM2.0rGO2.5}$ ,  $\text{AgM2.5rGO2.5}$  and  $\text{AgM3.0rGO2.5}$ , which means the mass ratios of  $\text{Ag}_3\text{PO}_4$ ,  $\text{MS}_2$  and rGO are 100:1.5:2.5, 100:2.0:2.5, 100:2.5:2.5 and 100:3.0:5.0, respectively. The  $\text{Ag}_3\text{PO}_4$  samples were prepared under the same condition and used as controls.

The morphologies of the as-prepared products were characterized using a scanning electron microscopy (SEM, ZEISS Merlin), and the phases of the obtained materials were recorded on a Bruker D8 Advance X-ray diffractometer with a Cu tube for generating  $\text{Cu K}\alpha$  radiation ( $\lambda = 1.5418 \text{ \AA}$ ). The surface electronic states were analyzed by using a Phi X-tool instrument, and the functional groups of the samples were determined using Fourier transform-infrared spectrometer (FT-IR, Tensore27, Bruker). The UV-vis diffuse reflectance spectra (DRS) were obtained on a Hitachi UV-3010 spectro- photometer by using  $\text{BaSO}_4$  as the reflectance standard. The fluorescence spectra were collected by using a fluorescence spectrophotometer (Hitachi, F-7000) with an excitation wavelength of 325 nm at wavelengths between 330–600 nm.

### 2.3. Photocatalytic degradation experiments and relative analysis

The photocatalytic degradation experiments were performed in a cylindrical quartz reactor surrounded by a cold trap and magnetic stirring continually to keep the photocatalyst evenly distributed. In a typical procedure, 100 mg of photocatalyst was added into 250 mL 4-nitrophenol (5 mg/L) aqueous solution, and the suspension was stirred in dark for 30 min to establish an adsorption-desorption equilibrium. Then, at given time interval of the irradiation (500 W Xenon lamp), 4.0 mL of the mixture was collected and centrifuged at 9000 rpm for 15 min to remove the photocatalyst for further analysis. 4-Nitrophenol concentration was monitored using a Shimadzu UV-2450 spectrophotometer at the wavelength of 318 nm and an Agilent 1260 high performance liquid chromatography (HPLC).

During photocatalytic degradation process, the intermediates were also separated and concentrated as previously described method [31]. The above concentrated sample was divided into equal portion. One portion was re-dissolved in 1 mL mixture solution of hexane and ethyl acetate (volume ratio = 1:1), and then quantified using a 7890B gas chromatography (GC) coupled with a 5977B mass spectrometer (MS) detector (Agilent Technologies, USA). Another portion was derived overnight at 25 °C using 50  $\mu\text{L}$   $N,\text{O}$ -bis- (trimethylsilyl)-

trifluoroacetamide (BSTFA) as derivation reagent for GC–MS detection equipped with a SH-Rxi-5Sil MS capillary column ( $30\text{ m} \times 0.25\text{ mm} \times 0.25\text{ }\mu\text{m}$ ). Temperature program of column was  $50\text{ }^\circ\text{C}$  for 1 min, rose to  $70\text{ }^\circ\text{C}$  at  $3\text{ }^\circ\text{C min}^{-1}$  holding for 1 min, rose to  $120\text{ }^\circ\text{C}$  at  $15\text{ }^\circ\text{C min}^{-1}$  holding for 1 min, and then rose to  $220\text{ }^\circ\text{C}$  at  $5\text{ }^\circ\text{C min}^{-1}$ . Mass spectra were recorded in electron ionization mode at an ion source temperature of  $230\text{ }^\circ\text{C}$ . Meanwhile, the 2,4-DNP peak was also separated from the mixture of intermediates by a preparative liquid chromatograph (Prep 150 LC), identified by NMR spectrometer (Bruker Avance III 400 spectrometer) with an operating frequency of 400.13 MHz (the details are shown in Supporting information) and double confirmed with authentic standard of 2,4-DNP. The nitrate ion ( $\text{NO}_3^-$ ) and nitrite ion ( $\text{NO}_2^-$ ) during the reaction process were detected by an ion chromatograph (882 Compact IC plus, Metrohm). The Total organic carbon concentrations were conducted on a Shimadzu TOC-v detector to validate the mineralization ratio of 4-nitrophenol. The  $\text{Ag}^+$  concentration in reaction solution was analyzed on an atomic absorption spectrometer (Z2000, Hitachi) using a silver hollow cathode lamp as light source.

#### 2.4. Reactive species analysis

The RSs in the photocatalytic degradation of 4-nitrophenol system were also detected with in-situ scavenging experiments. The hydroxyl radical ( $\text{OH}$ ), superoxide radical ( $\text{O}_2^-$ ), hole ( $\text{h}^+$ ) were captured using tert-butyl alcohol, *p*-benzoquinone and EDTA-2Na as scavengers (0.3 mM), respectively, and the increase or decrease of the degradation efficiency of 4-nitrophenol was used to investigate the contribution of RSs to the photocatalytic degradation.

### 3. Results and discussion

#### 3.1. Characterization of photocatalysts

The  $\text{Ag}_3\text{PO}_4@\text{MS}_2/\text{rGO}$  composite photocatalysts were synthesized using a liquid-exfoliation solvothermal method for the first time. The crystal types of as-prepared samples were examined by XRD to investigate their structural characteristics. As Fig. 1A shows, the characteristic peaks of  $\text{Ag}_3\text{PO}_4$  located at  $20.86^\circ$ ,  $29.68^\circ$ ,  $33.28^\circ$ ,  $36.55^\circ$ ,  $42.50^\circ$ ,  $47.78^\circ$ ,  $52.68^\circ$ ,  $55.00^\circ$ ,  $57.27^\circ$  and  $61.67^\circ$  are observed, which corresponds to the planes of (110), (200), (210), (211), (220), (310), (222), (320), (321) and (400) (PDF#06-0505), respectively [32,33]. The peak around  $11.2^\circ$  is ascribed to the characteristic peak of rGO, and it is noted that the peak intensity was obviously decreased after chemical modification. For the  $\text{Ag}_3\text{PO}_4@\text{WS}_2/\text{rGO}$  composite photocatalyst, an apparent peak observed at the position of  $14.4^\circ$  was ascribed to the (002) plane of  $\text{WS}_2$  (PDF#08-0237). A characteristic peak located at  $26.6^\circ$  in  $\text{Ag}_3\text{PO}_4@\text{MoS}_2/\text{rGO}$  corresponded to the (111) crystal faces of  $\text{MoO}_3$  (PDF#47-1081), which was attributed to surface of  $\text{MoS}_2$  being oxidized in the fabricating procedure. No obvious diffraction peaks of  $\text{MoS}_2$  were detected in the composite due to its low content (2 wt %). However, the following results of SEM and XPS could further identify the existence of  $\text{MoS}_2$ .

The morphologies of pure  $\text{Ag}_3\text{PO}_4$ ,  $\text{Ag}_3\text{PO}_4@\text{MoS}_2/\text{rGO}$  and  $\text{Ag}_3\text{PO}_4@\text{WS}_2/\text{rGO}$  composite photocatalyst were observed via SEM. The as-prepared pure  $\text{Ag}_3\text{PO}_4$  possesses an irregular cubic morphology with an average diameter of  $0.9\text{ }\mu\text{m}$  (Fig. 1B). The chemical modification of solvothermal method could make the  $\text{MS}_2/\text{rGO}$  hybrids closely coupling with  $\text{Ag}_3\text{PO}_4$  nano-sheets, and the  $\text{Ag}_3\text{PO}_4$  sheets were finer and more uniform than that of pure  $\text{Ag}_3\text{PO}_4$  (Fig. 1C and D), indicating that the contact structure was facilely obtained by this chemically modified method.

XPS spectra were carried out to further investigate the composition and chemical status of the elements of  $\text{Ag}_3\text{PO}_4@\text{MS}_2/\text{rGO}$  composite photocatalysts (Fig. 1E). The spectra of elements were studied by means of XPS-peak-differentiation-imitating analysis and the results are shown

in Fig. S1. As observed from the high resolution XPS spectra of  $\text{Ag}3\text{d}$ ,  $\text{O}1\text{s}$  and  $\text{P}2\text{p}$ , all the peaks are well consistent with the characteristics of  $\text{Ag}^+$ ,  $\text{P}5^+$ , and  $\text{O}2^-$  in  $\text{Ag}_3\text{PO}_4@\text{MS}_2/\text{rGO}$ , and the corresponding binding energy emerged variation relative to the value of pure  $\text{Ag}_3\text{PO}_4$  (Figs. S1A, S1B and S1C in Supporting information) [17]. However, the banding energy shifting of  $\text{Ag}3\text{d}$  and  $\text{P}2\text{p}$  were observed from the given figure, which verified the interaction of  $\text{Ag}_3\text{PO}_4$  and  $\text{MS}_2/\text{rGO}$  hybrids. From Fig. S1D, the  $\text{C}1\text{s}$  spectrum could be decomposed into three characteristic peaks, which were attributed to the following functional groups:  $\text{sp}2$  bounded carbon ( $\text{C}-\text{C}$ ,  $284.3\text{ eV}$ ), epoxy/hydroxyls ( $\text{C}-\text{O}$ ,  $285.9\text{ eV}$ ) and carboxyl ( $\text{O}-\text{C}=\text{O}$ ,  $288.1\text{ eV}$  or  $287.9\text{ eV}$ ). For  $\text{MoS}_2$  in  $\text{Ag}_3\text{PO}_4@\text{MoS}_2/\text{rGO}$  composite photocatalyst, the characteristic peaks of  $\text{Mo}3\text{d}3/2$ ,  $\text{Mo}3\text{d}5/2$ , and  $\text{S}2\text{s}$  were located at  $233.29$ ,  $230.82$  and  $226.9\text{ eV}$ , respectively, corresponding to  $\text{Mo}4^+$  and  $\text{S}2^-$  in  $\text{MoS}_2$  respectively (Fig. S1E in Supporting information) [34,35]. The peak around  $235.9\text{ eV}$  correspond to the characteristic peak of  $\text{Mo}6^+$ , indicating the existence of  $\text{MoO}_3$  in  $\text{Ag}_3\text{PO}_4@\text{MoS}_2/\text{rGO}$  due to parts of  $\text{MoS}_2$  sheets oxidized during the solvothermal process. From the XPS spectra of  $\text{Ag}_3\text{PO}_4@\text{WS}_2/\text{rGO}$ , the characteristic peaks of  $34.84$  and  $32.32\text{ eV}$  were observed, corresponding to the  $\text{W}4\text{f}5/2$  and  $\text{W}4\text{f}7/2$ , which were ascribed to the  $\text{W}4^+$  of  $\text{WS}_2$  [36,37]. The peaks of  $37.0$  and  $38.2\text{ eV}$  were ascribed to the  $\text{W}6^+$  of  $\text{WO}_3$  due to the oxidation of  $\text{WS}_2$ . The detailed atom ratios of each element in as-prepared photocatalysts were also calculated based on the XPS analysis, and the results are given in Table S1. The ratios of characteristic element indicated that all of the compounds concluding  $\text{Ag}_3\text{PO}_4$ , rGO,  $\text{MoS}_2$  and  $\text{WS}_2$  existed in the corresponding composite photocatalysts. The above XPS analysis demonstrated that the  $\text{Ag}_3\text{PO}_4$  nano-sheets could couple the  $\text{MS}_2/\text{rGO}$  hybrids with chemical interactions, which further verified by the SEM and XRD results.

Fig. 1F shows the FT-IR spectra of  $\text{Ag}_3\text{PO}_4@\text{MS}_2/\text{rGO}$  for investigating the functional group of the prepared photocatalysts. The characteristic peaks at  $1580$  and  $1385\text{ cm}^{-1}$  are assigned as the stretching vibrations of  $\text{C}=\text{C}$  and  $\text{C}-\text{OH}$  in rGO, respectively, according to references [38,39]. All the  $\text{Ag}_3\text{PO}_4$ -based samples have similar FT-IR peaks at  $541$ ,  $990$  and  $1072\text{ cm}^{-1}$ , which were ascribed to  $\text{P}-\text{O}$  stretching vibrations of  $\text{PO}_4^{3-}$  according to references [40,41]. The broaden absorption peak of  $1367\text{ cm}^{-1}$  was assigned to the  $\text{P}=\text{O}$  vibration of  $\text{PO}_4^{3-}$ . An apparent peak of  $1630\text{ cm}^{-1}$  appeared in both pure  $\text{Ag}_3\text{PO}_4$  and  $\text{Ag}_3\text{PO}_4@\text{MS}_2/\text{rGO}$  composite photocatalysts, which was assigned to  $\text{O}-\text{H}$  stretching vibrations of  $\text{H}_2\text{O}$ . In contrast to pure  $\text{Ag}_3\text{PO}_4$ ,  $\text{C}=\text{C}$  bond ( $1580\text{ cm}^{-1}$ ) increases slightly and the variation of  $\text{P}-\text{O}$  ( $1367\text{ cm}^{-1}$ ) was found in the spectra of  $\text{Ag}_3\text{PO}_4@\text{MS}_2/\text{rGO}$ , suggesting the intimate interaction between  $\text{Ag}_3\text{PO}_4$  and  $\text{MS}_2/\text{rGO}$  hybrids via the chemical bonding, as consisted with the SEM, XRD and XPS results.

The optical absorption properties of as-synthesized photocatalysts were also investigated with ultraviolet visible diffuse reflectance spectra (UV-vis DRS).  $\text{Ag}_3\text{PO}_4$  and  $\text{Ag}_3\text{PO}_4@\text{MS}_2/\text{rGO}$  composite photocatalysts both exhibit excellent absorption in the region less than  $520\text{ nm}$ , and specially, there is a distinct enhanced absorbance from approximately  $520$ – $800\text{ nm}$  for  $\text{Ag}_3\text{PO}_4@\text{MS}_2/\text{rGO}$  composite photocatalysts as compared with bare  $\text{Ag}_3\text{PO}_4$  (Fig. S2A in Supporting information). This prominent enhancement of the visible light absorption was attributed to the strong light harvesting property of  $\text{MS}_2/\text{rGO}$  hybrids, which could effectively enhance the utilization of photon energy, and simultaneously maintain high electron- transfer rate. The band gap values of as-prepared samples were calculated using Kubelka-Munk method [6]. According to this method, the bandgap energies ( $E_g$ ) of pure  $\text{Ag}_3\text{PO}_4$  without hydrothermal treatment, pure  $\text{Ag}_3\text{PO}_4$ ,  $\text{Ag}_3\text{PO}_4@\text{MoS}_2/\text{rGO}$  and  $\text{Ag}_3\text{PO}_4@\text{WS}_2/\text{rGO}$  have been calculated to be  $2.55$ ,  $2.52$ ,  $2.41$  and  $2.45\text{ eV}$ , respectively (Fig. S2B in Supporting information). The obvious bandgap narrowing suggested a favourable band matching and reasonable structure configuration of each component after  $\text{Ag}_3\text{PO}_4$  decorated with  $\text{MS}_2/\text{rGO}$  hybrids. These typical structures could efficiently contribute to the formation and transfer of

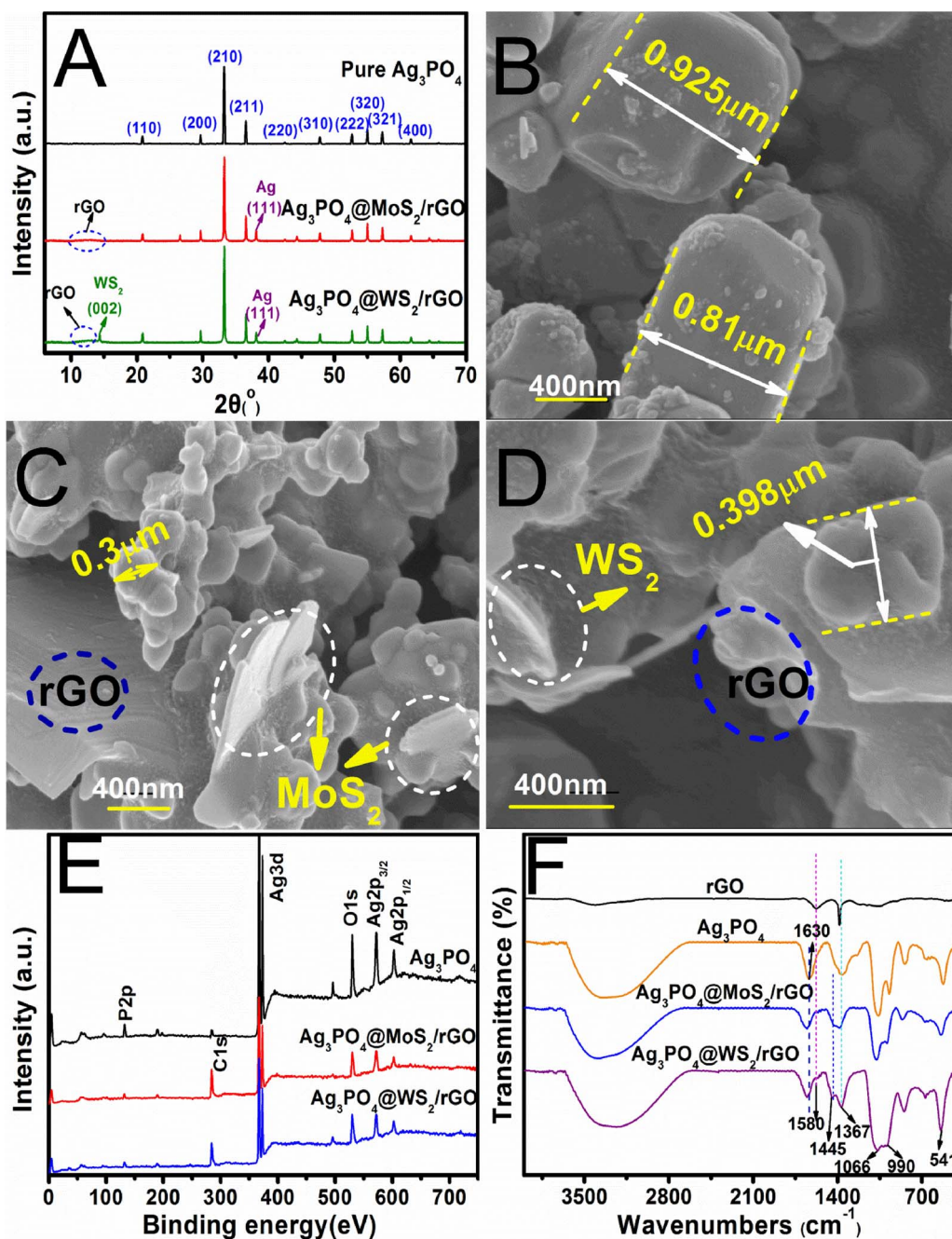


**Fig. 1.** Structure and composition analysis of  $\text{Ag}_3\text{PO}_4$  and  $\text{Ag}_3\text{PO}_4@\text{MS}_2/\text{rGO}$  composite photocatalysts: XRD spectra (A); SEM images of  $\text{Ag}_3\text{PO}_4$  (B),  $\text{Ag}_3\text{PO}_4@\text{MoS}_2/\text{rGO}$  (C) and  $\text{Ag}_3\text{PO}_4@\text{WS}_2/\text{rGO}$  (D); XPS curves (E) and IR spectra (F).

photogenerated charge carriers across the interface of  $\text{Ag}_3\text{PO}_4@\text{MS}_2/\text{rGO}$  composite photocatalysts.

### 3.2. Photocatalytic kinetics and photostability of photocatalysts

The photocatalytic performance of the as-synthesized  $\text{Ag}_3\text{PO}_4@\text{MS}_2/\text{rGO}$  composite photocatalysts was evaluated by decomposing 4-nitrophenol under simulated sunlight irradiation. Before irradiation, the reaction slurry of 4-nitrophenol and photocatalyst was magnetically stirred in dark for 30 min to achieve the adsorption–desorption equilibrium. The photocatalytic performance results are shown in Fig. S3. It was clear to see that the  $\text{Ag}_3\text{PO}_4@\text{MS}_2/\text{rGO}$  photocatalysts displayed higher adsorption ability toward 4-nitrophenol than pure  $\text{Ag}_3\text{PO}_4$ , which was beneficial for shortening the duration of adsorption between 4-nitrophenol and photocatalyst, resulting in enhancing the

subsequently photocatalytic degradation. From the photocatalytic experimental results, the photocatalytic degradation efficiencies of  $\text{Ag}_3\text{PO}_4@\text{MoS}_2/\text{rGO}$  ( $\text{AgMo3.0rGO2.5}$ ) and  $\text{Ag}_3\text{PO}_4@\text{WS}_2/\text{rGO}$  ( $\text{AgW3.0rGO2.5}$ ) reached 98.9% and 97.6%, respectively, which were higher than that of pure  $\text{Ag}_3\text{PO}_4$  (87%) towards 4-nitrophenol. Noted that, the  $\text{Ag}_3\text{PO}_4@\text{MoS}_2/\text{rGO}$  composite photocatalyst shows a little higher activity than that of  $\text{Ag}_3\text{PO}_4@\text{WS}_2/\text{rGO}$ , which was mainly attributed to the wider energy bandgap of  $\text{MoS}_2$  nanosheets than that of  $\text{WS}_2$  nanosheets, resulting in lower recombination of photogenerated electron/hole pairs for  $\text{Ag}_3\text{PO}_4@\text{MoS}_2/\text{rGO}$  than that of  $\text{Ag}_3\text{PO}_4@\text{WS}_2/\text{rGO}$  [42,43]. Further, the results showed that the efficiencies of  $\text{Ag}_3\text{PO}_4@\text{MS}_2/\text{rGO}$  photocatalysts were gradually enhanced with increase of the mass ratios of  $\text{MS}_2$ . Additionally, the influence of rGO with different mass ratio in the photocatalysts were also investigated and the results showed that the photocatalytic degradation efficiencies of

$\text{Ag}_3\text{PO}_4@\text{MoS}_2/\text{rGO}$  and  $\text{Ag}_3\text{PO}_4@\text{WS}_2/\text{rGO}$  decreased to 90% and 89%, respectively, when the mass ratio of rGO increasing from 2.5% to 5% (Table S2 in Supporting information). These results indicated that the appropriate amount of rGO could significantly improve the electron-transfer and photocatalytic activity of photocatalysts, but super-abundant rGO may not good for the separation efficiencies of photo-generated electron/hole pairs.

To further investigate the photocatalytic kinetic characteristics of different photocatalysts, the degradation curves of 4-nitrophenol are given in Fig. S4. From Fig. S4A, the photocatalytic degradation efficiencies of 4-nitrophenol over  $\text{Ag}_3\text{PO}_4@\text{MoS}_2/\text{rGO}$  and  $\text{Ag}_3\text{PO}_4@\text{WS}_2/\text{rGO}$  composite photocatalyst were higher than those of  $\text{Ag}_3\text{PO}_4$ ,  $\text{Ag}_3\text{PO}_4/\text{rGO}$ ,  $\text{Ag}_3\text{PO}_4/\text{MoS}_2$  and  $\text{Ag}_3\text{PO}_4/\text{WS}_2$  composite. In addition, the reaction kinetic constants for the degradation of 4-nitrophenol were calculated to be 0.1447, 0.1578, 0.1863, 0.1773, 0.2436 and 0.2000  $\text{min}^{-1}$ , respectively, for the samples of  $\text{Ag}_3\text{PO}_4$ ,  $\text{Ag}_3\text{PO}_4/\text{rGO}$ ,  $\text{Ag}_3\text{PO}_4/\text{MoS}_2$ ,  $\text{Ag}_3\text{PO}_4/\text{WS}_2$ ,  $\text{Ag}_3\text{PO}_4@\text{MoS}_2/\text{rGO}$  and  $\text{Ag}_3\text{PO}_4@\text{WS}_2/\text{rGO}$  (Fig. S4B and Table S3 in Supporting information). Namely, the degradation rates of 4-nitrophenol over  $\text{Ag}_3\text{PO}_4@\text{MoS}_2/\text{rGO}$  and  $\text{Ag}_3\text{PO}_4@\text{WS}_2/\text{rGO}$  composite photocatalyst were faster than that of pure  $\text{Ag}_3\text{PO}_4$ . Moreover, the photocatalytic kinetic constants of  $\text{Ag}_3\text{PO}_4@\text{MoS}_2/\text{rGO}$  were slightly higher than  $\text{Ag}_3\text{PO}_4@\text{WS}_2/\text{rGO}$ , which was possibly ascribed to the  $\text{MoS}_2$  with wider energy bandgap than that of  $\text{WS}_2$ . Especially, the photocatalytic performance of  $\text{Ag}_3\text{PO}_4/\text{MoS}_2$  and  $\text{Ag}_3\text{PO}_4/\text{WS}_2$  composites were more excellent than that of  $\text{Ag}_3\text{PO}_4/\text{rGO}$ , demonstrating that the compound interfaces between  $\text{Ag}_3\text{PO}_4$  and  $\text{MS}_2$  could not only improve the carrier transfer and separation but also increase the formation probability of R�s, resulting in enhancing the degradation rates of 4-nitrophenol. From above results, it was noted that the formation of contact structure between  $\text{Ag}_3\text{PO}_4$  and  $\text{MS}_2/\text{rGO}$  could tremendously promote the electron-transfer from  $\text{Ag}_3\text{PO}_4$  or  $\text{MS}_2$  to rGO, leading to lower recombination of photogenerated electron/hole pairs. Simultaneously, the Z-scheme PS between  $\text{MS}_2$  and  $\text{Ag}_3\text{PO}_4$  could effectively promote the separation of photogenerated electron/hole pairs, enhancing the utilization of photons.

The photocorrosion of  $\text{Ag}_3\text{PO}_4$  was the key problem to its practical application because the  $\text{Ag}_3\text{PO}_4$  is slightly soluble in water and the free  $\text{Ag}^+$  can be easily reduced into Ag by photoelectrons [44]. To investigate the contribution of  $\text{MS}_2/\text{rGO}$  to the photocatalytic stability of as-prepared photocatalysts, the recycle experiments for 4-nitrophenol degradation under simulated sunlight irradiation were also conducted in the presence of pure  $\text{Ag}_3\text{PO}_4$ ,  $\text{Ag}_3\text{PO}_4@\text{MoS}_2/\text{rGO}$  and  $\text{Ag}_3\text{PO}_4@\text{MoS}_2/\text{rGO}$  photocatalysts (Fig. S5 in Supporting information). It was found that the degradation efficiency of pure  $\text{Ag}_3\text{PO}_4$  decreased obviously after four successive cycles. In contrast, the  $\text{Ag}_3\text{PO}_4@\text{MS}_2/\text{rGO}$  composite photocatalysts display an excellent photostability and keep more than 98% photocatalytic degradation efficiency after four sequential cycles, indicating that the  $\text{MS}_2/\text{rGO}$  hybrids had great contribution to enhance the photocatalytic stability of  $\text{Ag}_3\text{PO}_4$ , due to inhibiting the recombination of photogenerated electron/hole pairs and the reduction of  $\text{Ag}_3\text{PO}_4$  to Ag by the photogenerated electrons.

To intuitively understand the stable state of different  $\text{Ag}_3\text{PO}_4$ -based photocatalysts, the leaching efficiencies of Ag element ( $\text{Ag}^+$  or metallic Ag) in aqueous phase from the photocatalysts were investigated during the 4-nitrophenol degradation processes. It was found that the concentrations of Ag element leached from pure  $\text{Ag}_3\text{PO}_4$ ,  $\text{Ag}_3\text{PO}_4/\text{MoS}_2$  and  $\text{Ag}_3\text{PO}_4/\text{WS}_2$  composites were sharply increased within 10 min as compared with  $\text{Ag}_3\text{PO}_4/\text{rGO}$ ,  $\text{Ag}_3\text{PO}_4@\text{MoS}_2/\text{rGO}$  and  $\text{Ag}_3\text{PO}_4@\text{WS}_2/\text{rGO}$  composite photocatalyst (Fig. S6). Namely, the coupling of rGO could effectively decrease the leaching of Ag element, then inhibit the decomposition of  $\text{Ag}_3\text{PO}_4$  and promote the electron-transfer of rGO within photocatalysts. Simultaneously, the leaching efficiencies of Ag element from  $\text{Ag}_3\text{PO}_4@\text{MoS}_2/\text{rGO}$  and  $\text{Ag}_3\text{PO}_4@\text{WS}_2/\text{rGO}$  composite photocatalyst were slower than that of  $\text{Ag}_3\text{PO}_4/\text{rGO}$  composite, indicating that Z-scheme electronic structure could also inhibit the

reduction of  $\text{Ag}^+$  due to consuming the photogenerated electrons. That is, high photocatalytic performance of  $\text{Ag}_3\text{PO}_4@\text{MoS}_2/\text{rGO}$  and  $\text{Ag}_3\text{PO}_4@\text{WS}_2/\text{rGO}$  composite photocatalyst as compared with  $\text{Ag}_3\text{PO}_4/\text{rGO}$ ,  $\text{Ag}_3\text{PO}_4/\text{MoS}_2$  and  $\text{Ag}_3\text{PO}_4/\text{WS}_2$  composites could be attributed to the slow leaching of Ag element as well as the timely and effectively transfer of photoinduced electrons of the surface of  $\text{Ag}_3\text{PO}_4$  to the surface of  $\text{MS}_2$  through rGO and then being consumed by the hole of  $\text{MS}_2$  due to special Z-Scheme electron transfer mechanism.

### 3.3. Possible mechanism of enhanced photocatalytic performance

To further clarify the mechanism of the enhanced photocatalytic activity of above system, the migration and recombination processes of photoinduced electron/hole pairs were systematically conducted because it closely related to the photocatalytic properties of catalyst [13,45]. Herein, photoluminescence (PL) spectra were performed to reveal the charge carrier transfer properties. As shown in Fig. S7A, the main emission peaks of  $\text{Ag}_3\text{PO}_4$  were found around 520 nm due to the recombination of photogenerated electron/hole pairs under the excitation at 325 nm, corresponding to radiative recombination of self-trapped excitons of  $\text{Ag}_3\text{PO}_4$  [24]. From the spectra, it was clear to see a relatively higher recombination of pure  $\text{Ag}_3\text{PO}_4$  as-compared with  $\text{Ag}_3\text{PO}_4@\text{MS}_2/\text{rGO}$  composites, indicated that  $\text{Ag}_3\text{PO}_4@\text{MS}_2/\text{rGO}$  composite photocatalysts possessed higher separation efficiency of electron/hole pairs.

These results can be also double confirmed by the frequently employed photoelectrochemical method used in many previous reports [24,46–48]. The electrochemical impedance spectra (EIS) test of as-synthesized pure  $\text{Ag}_3\text{PO}_4$ ,  $\text{Ag}_3\text{PO}_4@\text{MoS}_2/\text{rGO}$  and  $\text{Ag}_3\text{PO}_4@\text{WS}_2/\text{rGO}$  photocatalyst were also measured. It is because EIS can provide some information on the charge transfer resistance related to the diameter of the semicircle of Nyquist plots, where a smaller arc radius indicates a higher efficiency in charge transfer [15,27,49]. From Fig. S7B, the  $\text{Ag}_3\text{PO}_4@\text{MS}_2/\text{rGO}$  composite photocatalysts showed smaller semicircular diameter as compared with the pure  $\text{Ag}_3\text{PO}_4$ , demonstrating that the strong interaction between  $\text{Ag}_3\text{PO}_4$  and  $\text{MS}_2/\text{rGO}$  hybrids could efficiently improve the separation and transfer of photogenerated electron/hole pairs. Meanwhile, the  $\text{Ag}_3\text{PO}_4@\text{MoS}_2/\text{rGO}$  photocatalyst possessed higher separation efficiency of photo-generated electron/hole pairs than  $\text{Ag}_3\text{PO}_4@\text{WS}_2/\text{rGO}$  photocatalyst, which was also consistent with the characterization results of photocatalytic performance and PL analysis.

To better understand the mechanism of enhanced photocatalytic activity of  $\text{Ag}_3\text{PO}_4$  nano-sheets by  $\text{MS}_2/\text{rGO}$  hybrids, the electron-transfer mechanism was also illustrated. Normally, the bonding type of photocatalyst interfaces was closely related to the carrier transfer, and the chemical integration was commonly beneficial for the separation of photogenerated electron/hole pairs and the electron-transfer, which could obviously enhance the photocatalytic activity of photocatalyst. In addition, the type of interface structure could also make the radicals produced in many ways, leading to a deference in the photocatalytic mechanism. In  $\text{Ag}_3\text{PO}_4@\text{MS}_2/\text{rGO}$  photocatalyst system, Z-scheme electron-structure could be formed due to the matching energy-gap between  $\text{Ag}_3\text{PO}_4$  and  $\text{MS}_2$  [1,42,43]. Also, owing to the excellent electroconductibility of rGO, the carbon chains were surely acted as the electron-mediator in  $\text{Ag}_3\text{PO}_4@\text{MS}_2/\text{rGO}$  photocatalyst system, played an important role in the separation of photoinduced hole/electron pairs, and inhibited the reduction of  $\text{Ag}_3\text{PO}_4$  from electrons.

According to the above experimental results and discussion, a Z-scheme PS of electron-transfer mechanism was proposed [14]. As seen from Fig. 2, under the light excitation, the photoinduced electrons were transferred to the conduction band (CB) of  $\text{Ag}_3\text{PO}_4$  and  $\text{MS}_2$ , respectively, and left the holes in the valence band (VB) of  $\text{Ag}_3\text{PO}_4$  and  $\text{MS}_2$ . Subsequently, the accumulating electrons on CB of  $\text{Ag}_3\text{PO}_4$  would transfer to the VB of  $\text{MS}_2$  through the electron-mediator of rGO carbon chains, and consume the holes accumulated on the VB of  $\text{MS}_2$ . Two favorable effects could be

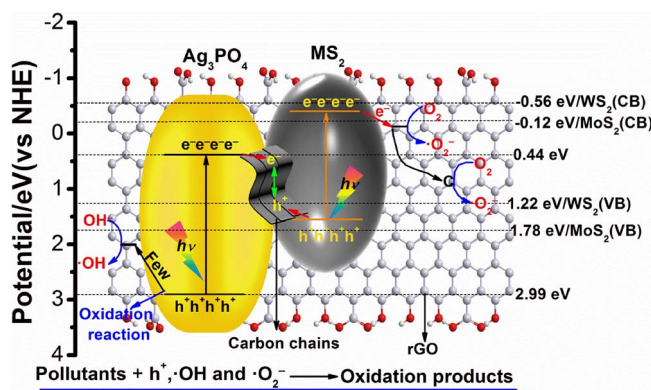


Fig. 2. Possible photogenerated charges transferring mechanism on  $\text{Ag}_3\text{PO}_4@\text{MS}_2/\text{rGO}$  composite photocatalysts.

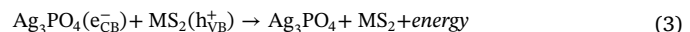
emerged from these analyses. One is, the electron-transfer on CB of  $\text{Ag}_3\text{PO}_4$  could obviously decrease  $\text{Ag}_3\text{PO}_4$  reduced into Ag, resulting in maintaining the crystal stability of  $\text{Ag}_3\text{PO}_4$  nano-sheets. And the consumption of holes accumulated on the VB of  $\text{MS}_2$  could also inhibit the oxidation of  $\text{MS}_2$ , leading to enhancing the photostability of  $\text{MS}_2$ . Thus, the formation of Z-scheme electron-structure between  $\text{Ag}_3\text{PO}_4$  and  $\text{MS}_2/\text{rGO}$  hybrids could effectively enhance the photocatalytic stability and activity of  $\text{Ag}_3\text{PO}_4@\text{MS}_2/\text{rGO}$  composite photocatalysts. Meanwhile, the adsorption ability to 4-nitrophenol was another importance of favorable effects because the pre-adsorption of photocatalyst to 4-nitrophenol will significantly shorten the diffusion time of 4-nitrophenol to surface active sites of the  $\text{Ag}_3\text{PO}_4@\text{MS}_2/\text{rGO}$  composite photocatalysts, which was also the important reason for the rapid photocatalytic degradation of 4-nitrophenol. Hence, the excellent electron-structure and high adsorption ability of organic pollutants onto photocatalysts were two important affecting-parameters for higher degradation efficiencies of organic pollutants in the practical application.

### 3.4. Photocatalytic degradation mechanism of 4-nitrophenol onto $\text{Ag}_3\text{PO}_4@\text{MS}_2/\text{rGO}$ photocatalyst

To further probe the contributions of RSs in the photocatalytic degradation of 4-nitrophenol in this work, tert-butyl alcohol, EDTA-2Na and p-benzoquinone were employed as the scavengers to identify the involving of  $\cdot\text{OH}$ ,  $\text{h}^+$  and  $\cdot\text{O}_2^-$ , respectively [44,50,51]. As Fig. 3 shows, the photocatalytic degradation performance of  $\text{Ag}_3\text{PO}_4@\text{MS}_2/\text{rGO}$  almost remained unchanged when tert-butyl alcohol was added into the reaction solution systems, suggesting that  $\cdot\text{OH}$  played a negligible role in this photocatalytic process. In contrast, when EDTA-2Na or p-benzoquinone was added into the reaction system, the photocatalytic degradation efficiencies were greatly inhibited, suggesting that the  $\text{h}^+$  and  $\cdot\text{O}_2^-$  were the dominated RSs. The generation of  $\text{h}^+$  was mainly attributed to high oxidative potential of  $\text{Ag}_3\text{PO}_4$ , and the  $\cdot$

$\text{O}_2^-$  was generated through adsorbed  $\text{O}_2$  reacting with photoinduced electrons. These results revealed that the  $\text{h}^+$  and  $\cdot\text{O}_2^-$  mediated the photocatalytic degradation of 4-nitrophenol by  $\text{Ag}_3\text{PO}_4@\text{MS}_2/\text{rGO}$  composite photocatalysts.

Based on these results, the formation and transfer mechanism of RSs would be proposed as following: Firstly, the accumulated holes on the VB of  $\text{Ag}_3\text{PO}_4$  could directly participate in the photocatalytic oxidation of 4-nitrophenol and very limited holes were then transformed into  $\cdot\text{OH}$  and involved in the oxidation of 4-nitrophenol; secondly, the CB bottom of  $\text{MS}_2$  was more negative than that of  $\text{O}_2/\cdot\text{O}_2^-$ , and the adsorbed  $\text{O}_2$  could react with electrons to form  $\cdot\text{O}_2^-$ , which could also participate in the photo-oxidation reaction of 4-nitrophenol; In addition, the electrons from the CB of  $\text{Ag}_3\text{PO}_4$  or  $\text{MS}_2$  could be transferred into the active sites of rGO through the carbon chains of rGO, and reacted with the active  $\text{O}_2$  into  $\cdot\text{O}_2^-$ , leading to enhancing the photocatalytic activity and the stability of as-synthesized composite photocatalysts. The  $\cdot\text{O}_2^-$  could also transfer into  $\cdot\text{OH}$  through a series of reaction [13], which participated in the photocatalytic oxidation of 4-nitrophenol. The major reactions that occur in this study can be summarized in reactions Eqs. (1)–(5) [10,13,52].



Of course, the above discussed RSs can initial the degradation of 4-nitrophenol and then mediate the further degradation of 4-nitrophenol as well as its degradation intermediates. Thus, the analysis of intermediates was the key step to investigate the photocatalytic degradation mechanism of 4-nitrophenol. Herein, three main intermediates were detected and identified as p-benzoquinone, hydroquinone and 2,4-DNP with and without BSTFA derivatization. The intermediates are also qualitatively validated in this work by the comparison of mass spectrometry with corresponding authentic standards. The chemical structure and retention time of the three intermediates are summarized in Table S4, and the corresponding mass spectra are also displayed in Fig. S8. Note that p-benzoquinone was found only without BSTFA derivatization, while the other two intermediates were identified both with and without BSTFA derivatization.

To better understand the environmental fate of 4-nitrophenol in water environments, its possible degradation pathways were also proposed based on above intermediates identified. The detailed pathway of intermediates during 4-nitrophenol degradation process on  $\text{Ag}_3\text{PO}_4@\text{MS}_2/\text{rGO}$  is also illustrated in Scheme 1. According to the above analysis, the photogenerated  $\text{h}^+$  and  $\cdot\text{O}_2^-$  were the main RSs in this photocatalytic degradation system. Due to the strong oxidation capacities

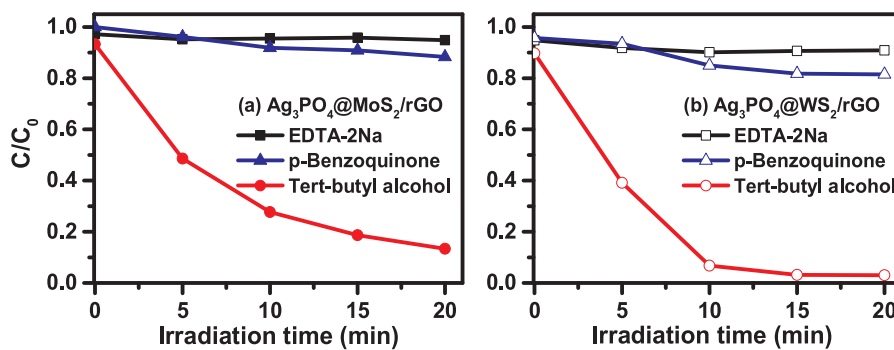
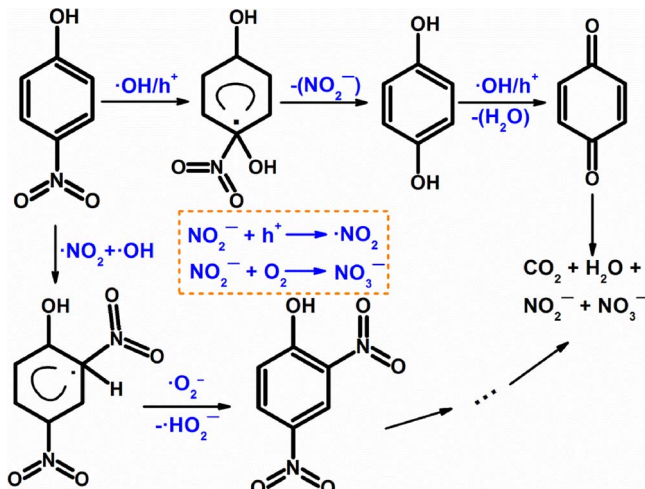


Fig. 3. Radicals trapping experiments for the degradation of 4-nitrophenol conducted on  $\text{Ag}_3\text{PO}_4@\text{MoS}_2/\text{rGO}$  (a) and  $\text{Ag}_3\text{PO}_4@\text{WS}_2/\text{rGO}$  (b). (Dosage of photocatalyst, 0.4 g/L; reaction time, 20 min; concentration of 4-nitrophenol, 5 mg/L).



**Scheme 1.** Possible photocatalytic degradation pathway of 4-nitrophenol catalyzed by  $\text{Ag}_3\text{PO}_4@\text{MoS}_2/\text{rGO}$  photocatalysts.

of  $\text{h}^+$ , the denitration reaction of 4-nitrophenol could be first occurred in the initial photocatalytic process, resulting in the free  $\text{NO}_2^-$  rapidly accumulated in the reaction system. Besides, the  $\cdot\text{O}_2^-$  could transform into  $\cdot\text{OH}$  via a series of radical reactions. Thus, the 4-nitrophenol undergoes the reaction with  $\cdot\text{OH}$  as similar with the electrophilic attack reaction due to the oxidation of  $\cdot\text{OH}$ , resulting in the formation of hydroquinone. Simultaneously, the produced hydroquinone was also easily oxidized by  $\cdot\text{O}_2^-$  or  $\text{h}^+$  to form p-benzoquinone according the early references [31,53]. It is surprised that 2,4-DNP was also obtained during the photocatalytic oxidation of 4-nitrophenol in this work, and many previous research also confirm this nitration reaction of 4-nitrophenol [54–56]. It is because, in this typical process, the  $\cdot\text{OH} + \cdot\text{NO}_2$  may act as the nitrating agent, which played a key role in the formation of 2,4-DNP [57]. The possible source of nitrogen dioxide in the aqueous system is the oxidation of  $\text{NO}_2^-$  produced during the denitration reaction of 4-nitrophenol. Herein, the  $\text{h}^+$  is oxidizing agent, but its reactivity is different from that of  $\cdot\text{OH}$ . The premise of the formation of 2,4-DNP was that the  $\text{h}^+$  of irradiated  $\text{Ag}_3\text{PO}_4$  can oxidize the  $\text{NO}_2^-$  much faster than 4-nitrophenol. Thus, the electron-donor property of hydroxyl group on the benzene ring facilitates the electrophilic attack of the free  $\text{NO}_2$  radicals on the ortho-position, leading to the free  $\text{NO}_2$  rapidly coupled with 4-nitrophenol to form 2,4-DNP according to the references [53–55]. To further confirm the formation of 2,4-DNP during the photocatalytic degradation of 4-nitrophenol, the degradation intermediates peak of 2,4-DNP in HPLC effluent was separated and identified by NMR spectrometer. Furthermore, the NMR spectra of C spectrum and H spectrum for preparative 2,4-DNP with its authentic standards were compared respectively, and the detailed results are shown in Figs. S9a and S9b. From the data in Fig. S9, the conclusion is double confirmed that 2,4-DNP was really formed in this degradation system.

To better understand the correlation of 4-nitrophenol and its degradation intermediates, the concentration of  $\text{NO}_2^-$ ,  $\text{NO}_3^-$ , 2,4-DNP and p-benzoquinone were also monitored by IC and HPLC using a standard curve method (Figs. S10 and S4). The results showed that the concentrations of  $\text{NO}_2^-$ ,  $\text{NO}_3^-$  and 2,4-DNP rapidly increased with the degradation of 4-nitrophenol within 10 min, which was attributed to the denitration and nitration of 4-nitrophenol, respectively. It was noted that the generation efficiencies of  $\text{NO}_2^-$  was faster than that of  $\text{NO}_3^-$  because the  $\text{NO}_3^-$  was generated from the oxidation of  $\text{NO}_2^-$  with  $\text{O}_2$ . For  $\text{Ag}_3\text{PO}_4$ ,  $\text{Ag}_3\text{PO}_4@\text{MoS}_2/\text{rGO}$  and  $\text{Ag}_3\text{PO}_4@\text{WS}_2/\text{rGO}$ , the concentration of 2,4-DNP firstly increased and then decreased as the photocatalytic reaction progress. In contrast, the 2,4-DNP was not generated in  $\text{Ag}_3\text{PO}_4/\text{rGO}$  photocatalysis system, which demonstrated

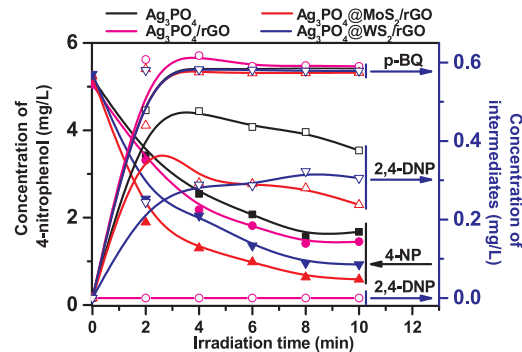


**Fig. 4.** Variation curves of major intermediates during photocatalytic degradation of 4-nitrophenol catalyzed by pure  $\text{Ag}_3\text{PO}_4$ ,  $\text{Ag}_3\text{PO}_4/\text{rGO}$ ,  $\text{Ag}_3\text{PO}_4@\text{MoS}_2/\text{rGO}$  and  $\text{Ag}_3\text{PO}_4@\text{WS}_2/\text{rGO}$  composite photocatalyst (Dosage of photocatalyst, 0.1 g/L; reaction time, 10 min; concentration of 4-nitrophenol, 5 mg/L) (4-NP: 4-nitrophenol; p-BQ: p-benzoquinone; 2,4-DNP: 2,4-dinitrophenol).

that the surface holes of  $\text{Ag}_3\text{PO}_4/\text{rGO}$  oxidized the 4-nitrophenol much faster than  $\text{NO}_2^-$ . This typical process could also explain the generation rate of  $\text{NO}_2^-$  on  $\text{Ag}_3\text{PO}_4/\text{rGO}$  was higher than that of pure  $\text{Ag}_3\text{PO}_4$ ,  $\text{Ag}_3\text{PO}_4@\text{MoS}_2/\text{rGO}$  and  $\text{Ag}_3\text{PO}_4@\text{WS}_2/\text{rGO}$  composite photocatalyst. From the variation of total nitrogen in aqueous solution, the total nitrogen was sharply decreased with the photocatalytic degradation of 4-nitrophenol, which could be the generated  $\text{NO}_2^-$ ,  $\text{NO}_3^-$  or  $\cdot\text{NO}_2$  and accumulated on the surface of photocatalysts with the effect of surface electrical field, and subsequently diffused into the aqueous phase. It was noted that the p-benzoquinone was produced by using all kinds of photocatalysts because the hydroquinone was instable intermediates and could be easily oxidized into p-benzoquinone by RSs such as  $\text{h}^+$  and very limited  $\cdot\text{OH}$  [53] (Fig. 4).

To further investigate the environment application effectiveness of composite photocatalysts, the extent of mineralization of 4-nitrophenol solution is measured. Fig. 5 shows the mineralization curves of 4-nitrophenol during the degradation process by  $\text{Ag}_3\text{PO}_4$ ,  $\text{Ag}_3\text{PO}_4/\text{rGO}$ ,  $\text{Ag}_3\text{PO}_4/\text{MoS}_2$ ,  $\text{Ag}_3\text{PO}_4/\text{WS}_2$ ,  $\text{Ag}_3\text{PO}_4@\text{MoS}_2/\text{rGO}$  and  $\text{Ag}_3\text{PO}_4@\text{WS}_2/\text{rGO}$  composite photocatalyst. For pure  $\text{Ag}_3\text{PO}_4$ , under simulated sunlight irradiation for 1 h, approximately 26.7% of carbon contents in 4-nitrophenol solution is mineralized and completely converted into  $\text{CO}_2$ , which are lower than those of  $\text{Ag}_3\text{PO}_4/\text{rGO}$  (27.6%),  $\text{Ag}_3\text{PO}_4/\text{MoS}_2$  (34.5%),  $\text{Ag}_3\text{PO}_4/\text{WS}_2$  (31.1%),  $\text{Ag}_3\text{PO}_4@\text{MoS}_2/\text{rGO}$  (38.8%),  $\text{Ag}_3\text{PO}_4@\text{WS}_2/\text{rGO}$  (35.5%), indicating the enhanced photocatalytic performance of  $\text{Ag}_3\text{PO}_4$  with the modification of rGO, MS<sub>2</sub>, MS<sub>2</sub>/rGO hybrids. It is also noted that  $\text{Ag}_3\text{PO}_4@\text{MS}_2/\text{rGO}$  composite photocatalysts show higher mineralization efficiencies than that of  $\text{Ag}_3\text{PO}_4/\text{rGO}$ .

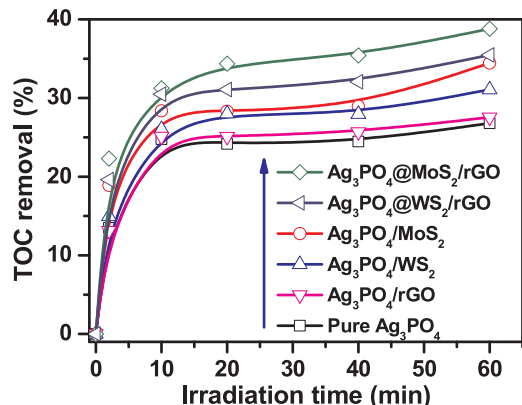


**Fig. 5.** TOC removal efficiency of 4-nitrophenol by pure  $\text{Ag}_3\text{PO}_4$ ,  $\text{Ag}_3\text{PO}_4/\text{MoS}_2$ ,  $\text{Ag}_3\text{PO}_4/\text{WS}_2$ ,  $\text{Ag}_3\text{PO}_4/\text{rGO}$ ,  $\text{Ag}_3\text{PO}_4@\text{MoS}_2/\text{rGO}$  and  $\text{Ag}_3\text{PO}_4@\text{WS}_2/\text{rGO}$  changed with different irradiation time (Dosage of photocatalyst, 0.1 g/L; reaction time, 60 min; concentration of 4-nitrophenol, 5 mg/L).

rGO, Ag<sub>3</sub>PO<sub>4</sub>/MoS<sub>2</sub> and Ag<sub>3</sub>PO<sub>4</sub>/WS<sub>2</sub> because the typical Z-scheme electronic structure was formed between MS<sub>2</sub>/rGO hybrids and Ag<sub>3</sub>PO<sub>4</sub> nano-sheets, which was very consistent with above-mentioned photocatalytic experiment results.

#### 4. Conclusions

In conclusion, a chemically modified process called liquid-exfoliation solvothermal method was employed for fabricating the ternary system of Ag<sub>3</sub>PO<sub>4</sub>@MS<sub>2</sub>/rGO composite photocatalysts for the first time. Typically, the photocatalytic activity and the stability of Ag<sub>3</sub>PO<sub>4</sub> nano-sheets were apparently enhanced by coupling with MS<sub>2</sub>/rGO hybrids for the photocatalytic degradation of 4-nitrophenol. The enhanced photocatalytic activity and the stability were closely related to the synergistic effect of Ag<sub>3</sub>PO<sub>4</sub> nanosheets and MS<sub>2</sub>/rGO hybrids, and the formed Z-scheme PS could efficiently promote the separation and transfer of photogenerated electron/hole pairs, which was supported by photocatalytic experiment, electrochemical impedance spectra and PL spectra, respectively. The radicals trapping experiments demonstrated that the holes and ·O<sub>2</sub><sup>−</sup> played the dominated role during the photocatalytic degrading 4-nitrophenol. Moreover, the intermediates of 4-nitrophenol were also conducted by GC-MS and the photocatalytic mechanism was also clearly discussed. These results demonstrated that the 4-nitrophenol was firstly interacted with h<sup>+</sup> and degraded into NO<sub>2</sub><sup>−</sup>, hydroquinone, and subsequently transformed into NO<sub>3</sub><sup>−</sup>, 2,4-DNP, p-benzoquinone and other small organic molecules. The intermediate products were finally interacted with h<sup>+</sup> and ·O<sub>2</sub><sup>−</sup> for complete mineralization. This work may provide practical applicability of designing photocatalysts with high efficiency and stability for the removal of organic pollutants, which was the promising technique for environmental remediation.

#### Acknowledgment

This work was supported by the National Natural Science Foundation of China (21425015, 21376099, 21546002, 41373102, 21607028).

#### Appendix A. Supplementary data

Supplementary material related to this article can be found, in the online version, at doi:<https://doi.org/10.1016/j.apcatb.2018.03.006>.

#### References

- Z.G. Yi, J.H. Ye, N. Kikugawa, T. Kako, S.X. Ouyang, H. Stuart-Williams, H. Yang, J.Y. Cao, W.J. Luo, Z.S. Li, Y. Liu, R.L. Withers, *Nat. Mater.* 9 (2010) 559–564.
- J.J. Guo, S.X. Ouyang, P. Li, Y.J. Zhang, T. Kako, J.H. Ye, *Appl. Catal. B: Environ.* 134–135 (2013) 286–292.
- C.S. Kuo, C.F. Lin, P.K. Andy Hong, *Water Res.* 74 (2015) 1–9.
- W.J. Wang, G.Y. Li, D.H. Xia, T.C. An, H.J. Zhao, P.K. Wong, *Environ. Sci.: Nano* 4 (2017) 782–799.
- Y.P. Bi, S.X. Ouyang, N. Umezawa, J.Y. Cao, J.H. Ye, *J. Am. Chem. Soc.* 133 (2011) 6490–6492.
- X.J. Guan, L.J. Guo, *ACS Catal.* 4 (2014) 3020–3026.
- Y.Y. Bu, Z.Y. Chen, C.J. Sun, *Appl. Catal. B: Environ.* 179 (2015) 363–371.
- W.C. Peng, X. Wang, X.Y. Li, *Nanoscale* 6 (2014) 8311–8317.
- Y.P. Bi, H.Y. Hu, S.X. Ouyang, Z.B. Jiao, G.X. Lu, J.H. Ye, *J. Mater. Chem.* 18 (2012) 14272–14275.
- T.Y. Xu, R.L. Zhu, J.X. Zhu, X.L. Liang, Y. Liu, Y. Xu, H.P. He, *Catal. Sci. Technol.* 6 (2016) 4116–4123.
- C.N. Tang, E.Z. Liu, J. Wan, X.Y. Hu, J. Fan, *Appl. Catal. B: Environ.* 181 (2016) 707–715.
- Y.J. Li, L.M. Yu, N. Li, W.F. Yan, X.T. Li, *J. Colloid Interface Sci.* 450 (2015) 246–253.
- B.K. Liu, Y.F. Xue, J.T. Zhang, B. Han, J. Zhang, X.Y. Suo, L.L. Mu, H.Z. Shi, *Environ. Sci.: Nano* 4 (2017) 255–264.
- P. Zhou, J.G. Yu, M. Jaroniec, *Adv. Mater.* 26 (2014) 4920–4935.
- Y.M. He, L.H. Zhang, B.T. Teng, M.H. Fan, *Environ. Sci. Technol.* 49 (2015) 649–656.
- X.F. Yang, Z.P. Chen, J.S. Xu, H. Tang, K.M. Chen, Y. Jiang, *ACS Appl. Mater. Interfaces* 7 (2015) 15285–15293.
- P.F. Tan, X. Chen, L.D. Wu, Y.Y. Shang, W.W. Liu, J. Pan, X. Xiong, *Appl. Catal. B: Environ.* 202 (2017) 326–334.
- H.J. Yu, Y. Yu, J.H. Liu, P.Y. Ma, Y.C. Wang, F. Zhang, Z.Y. Fu, *J. Mater. Chem. A* 3 (2015) 19439–19444.
- W.P. Zhang, X.Y. Xiao, Y. Li, X.Y. Zeng, L.L. Zheng, C.X. Wan, *RSC Adv.* 6 (2016) 33705–33712.
- X.Q. Hao, Z.L. Jin, H. Yang, G.X. Lu, Y.P. Bi, *Appl. Catal. B: Environ.* 210 (2017) 45–56.
- B. Mahler, V. Hoepfner, K. Liao, G.A. Ozin, *J. Am. Chem. Soc.* 136 (2014) 14121–14127.
- W.K. Ho, J.C. Yu, J. Lin, J.G. Yu, P.S. Li, *Langmuir* 20 (2004) 5865–5869.
- N. Shao, J.N. Wang, D.D. Wang, P. Corvini, *Appl. Catal. B: Environ.* 203 (2017) 964–978.
- J. Wan, X. Du, E.Z. Liu, Y. Hu, J. Fan, X.Y. Hu, *J. Catal.* 345 (2017) 281–294.
- X.F. Yang, J.L. Qin, Y. Jiang, K.M. Chen, X.H. Yan, D. Zhang, R. Li, H. Tang, *Appl. Catal. B: Environ.* 166–167 (2015) 231–240.
- L.H. Feng, L.R. Kong, Z.Y. Ji, Y. Wang, X.P. Shen, S.Q. Cheng, S.K. Wu, *Nano* 12 (2017) 1750013.
- F. Chen, Q. Yang, X.M. Li, G.M. Zeng, D.B. Wang, C.G. Niu, J.W. Zhao, H.X. An, T. Xie, Y.C. Deng, *Appl. Catal. B: Environ.* 200 (2017) 330–342.
- J.Y. Chen, H.M. Zhang, P.R. Liu, Y.B. Li, X.L. Liu, G.Y. Li, P.K. Wong, T.C. An, H.J. Zhao, *Appl. Catal. B: Environ.* 168–169 (2015) 266–273.
- W.S. Hummers Jr., R.E. Offeman, *J. Am. Chem. Soc.* 80 (1958) 1339.
- W.P. Zhang, X.Y. Xiao, X.Y. Zeng, Y. Li, L.L. Zheng, C.X. Wan, *J. Alloys Comp.* 685 (2016) 774–783.
- W.B. Zhang, X.M. Xiao, T.C. An, Z.G. Song, J.F. Fu, G.Y. Sheng, M.C. Cui, *J. Chem. Technol. Biotechnol.* 78 (2003) 788–794.
- X.X. Chen, X.T. Huang, Z.G. Yi, *Chem. Eur. J.* 20 (2014) 17590–17596.
- J. Cao, B.D. Luo, H.L. Lin, B.Y. Xu, S.F. Chen, *J. Hazard. Mater.* 217–218 (2012) 107–115.
- L.H. Yuwen, F. Xu, B. Xue, Z.M. Luo, Q. Zhang, B.Q. Bao, S. Su, L.X. Weng, W. Huang, L.H. Wang, *Nanoscale* 6 (2014) 5762–5769.
- G.P. Chen, D.M. Li, F. Li, Y.Z. Fan, H.F. Zhao, Y.H. Luo, R.C. Yu, Q.B. Meng, *Appl. Catal. A: Gen.* 443–444 (2012) 138–144.
- J.P. Zou, J. Ma, J.M. Luo, J. Yu, J.K. He, Y.T. Meng, Z. Luo, S.K. Bao, H.L. Liu, S.L. Luo, X.B. Luo, T.C. Chen, S.L. Suib, *Appl. Catal. B: Environ.* 179 (2015) 220–228.
- Y. Hou, Y. Zhu, Y. Xu, X. Wang, *Appl. Catal. B: Environ.* 156 (2014) 122–127.
- B. Chai, J. Li, Q. Xu, *Ind. Eng. Chem. Res.* 53 (2014) 8744–8752.
- S. Bai, X.P. Shen, H.W. Lv, G.X. Zhu, C.L. Bao, Y.X. Shan, *J. Colloid Interface Sci.* 405 (2013) 1–9.
- E. Akbarzadeh, S.R. Setayesh, M.R. Gholami, *RSC Adv.* 6 (2016) 14909–14915.
- C. Cui, Y.P. Wang, D.Y. Liang, W. Cui, H.H. Hu, B.Q. Lu, S. Xu, X.Y. Li, C. Wang, Y. Yang, *Appl. Catal. B: Environ.* 158–159 (2014) 150–160.
- S. Park, N. Mutz, T. Schultz, S. Blumstengel, A. Han, A. Aljbar, L.J. Li, E.J.W. List-Kratochvil, P. Amsalem, N. Koch, *2D Materials* 5 (2018) 025003.
- D. Xu, P. Xu, Y. Zhu, W. Peng, Y. Li, G. Zhang, F. Zhang, T.E. Mallouk, X. Fan, *ACS Appl. Mater. Interfaces* 10 (2018) 2810–2818.
- T. Cai, Y.T. Liu, L.L. Wang, S.Q. Zhang, Y.X. Zeng, J.L. Yuan, J.H. Ma, W.Y. Dong, C.B. Liu, S.L. Luo, *Appl. Catal. B: Environ.* 208 (2017) 1–13.
- J.W. Xu, Z.D. Gao, K. Han, Y.M. Liu, Y.Y. Song, *ACS Appl. Mater. Interfaces* 6 (2014) 15122–15131.
- J.Q. Li, H. Yuan, Z.F. Zhu, *J. Colloid Interface Sci.* 462 (2016) 382–388.
- C.X. Zhang, K. Yu, Y.J. Feng, Y. Chang, T. Yang, Y. Xuan, D. Lei, L.L. Lou, S.X. Liu, *Appl. Catal. B: Environ.* 210 (2017) 77–87.
- L. Liu, Y.H. Qi, J.R. Lu, S.L. Lin, W.J. An, Y.H. Liang, W.Q. Cui, *Appl. Catal. B: Environ.* 183 (2016) 133–141.
- X.Q. Liu, W.J. Chen, H. Jiang, *Chem. Eng. J.* 308 (2017) 889–896.
- L. Zhou, W. Zhang, L. Chen, H.P. Deng, *J. Colloid Interface Sci.* 487 (2017) 410–417.
- Q. Zhu, X.H. Hu, M.S. Stanislaus, N. Zhang, R.D. Xiao, N. Liu, Y.N. Yang, *Sci. Total Environ.* 577 (2017) 236–244.
- H.L. Lin, H.F. Ye, B.Y. Xu, J. Cao, S.F. Chen, *Catal. Commun.* 37 (2013) 55–59.
- L.X. Yang, S.L. Luo, Y. Li, Y. Xiao, Q. Kang, Q.Y. Cai, *Environ. Sci. Technol.* 44 (2010) 7641–7646.
- D. Vione, V. Maurino, C. Minero, E. Pelizzetti, *Environ. Sci. Technol.* 39 (2005) 7921–7931.
- Y.F. Ji, L. Wang, M.D. Jiang, J.H. Lu, C. Ferronato, J.M. Chovelon, *Wat. Res.* 123 (2017) 249–257.
- Y.F. Ji, Y.Y. Shi, L. Wang, J.H. Lu, *Chem. Eng. J.* 315 (2017) 591–597.
- P. Barzaghi, H. Herrmann, *Phys. Chem. Chem. Phys.* 4 (2002) 3669–3675.